Optics and Lasers in Engineering 193 (2025) 109100

Contents lists available at ScienceDirect

Optics and Lasers in Engineering

journal homepage: www.elsevier.com/locate/optlaseng

High-resolution and real-time non-line-of-sight imaging based on spatial correlation

Wenjun Zhang [a], Shuo Zhu [b], Lijia Chen [a], Lianfa Bai [a], Edmund Y. Lam [b], Enlai Guo [a,*], Jing Han [a,*]

[a] Jiangsu Key Laboratory of Visual Sensing and Intelligent Perception, Nanjing University of Science and Technology, Nanjing 210094, China

[b] Department of Electrical and Electronic Engineering, The University of Hong Kong, Pokfulam, Hong Kong Special Administrative Region of China

ARTICLE INFO

Keywords:
Non-line-of-sight imaging
High-resolution
Real-time inference

ABSTRACT

Non-line-of-sight (NLOS) imaging technique has broad application prospects in fields such as autonomous driving and robotic vision. Among the existing NLOS imaging methods, the scan-free methods allow rapid data acquisition. However, the imaging resolution is limited by the system's temporal jitter and the number of pixels in the array detector, and the real-time recovery of complex dynamic scenes is still a major challenge. Here, based on the temporal and spatial broadening of the signal and the evolution characteristics of optical transmission fields, we establish the three-dimensional blur kernel and the forward evolution model under scan-free conditions. Subsequently, leveraging the spatial correlation between adjacent detection region information, we propose a resampling method to obtain high-resolution data information with fine collection. Combining this with three-dimensional blur kernel modeling makes high-resolution imaging of hidden targets realized through model inversion. Our method improves the lateral resolution of the imaging results and enables the reconstruction of dynamically complex scenes. We demonstrate high-resolution NLOS imaging at 5 frames per second for dynamic scenes, providing valuable insights for practical applications of NLOS imaging.

1. Introduction

Non-line-of-sight (NLOS) imaging can restore hidden scenes beyond the line of sight by analyzing indirect reflected light scattered from the surrounding environment, and it has applications in fields such as robotic vision, autonomous driving, medical imaging, disaster assistance, and cave exploration [1–7]. In recent years, NLOS imaging has garnered considerable attention, and various solutions based on different principles have been proposed. Typical methods include speckle correlation [8,9], wavefront shaping [10], acoustic imaging [11], thermal imaging [12], and transient imaging techniques [13–16,6,17]. Among these, transient imaging methods have become a focal point of research in recent years due to their three-dimensional reconstruction abilities and wide application prospects.

In the transient NLOS imaging system, the pulse laser is used for active illumination, and the time-resolved detector can collect the time response information diffusely reflected from the hidden scene to the relay wall. However, a single time-of-flight (ToF) measurement often suffers from significant errors. Therefore, the detector is typically combined with a time-correlated single-photon counting module as the detection system to count the sampled ToF and generate a time distribution histogram [18]. After collecting sufficient signals, an appropriate computational method is then used to decode the signals [19]. The earliest NLOS methods use a streak camera and reconstruct the 5D data collected based on the back-projection algorithm [13,20]. However, such systems necessitate the simultaneous scanning of both the light source and the camera, resulting in prolonged acquisition times and complex reconstruction processes. Subsequent work has proposed error back-projection algorithms [21] and fast back-projection algorithms [22] based on the original back-projection algorithm, enhancing imaging resolution and speed respectively. To simplify the acquisition process, the method of transmitting and receiving coaxial is adopted, which simplifies the forward model of NLOS imaging. Based on the propagation process of geometric optics, a light-cone transform (LCT) algorithm based on deconvolution process is designed, which can achieve high-fidelity reconstruction of the target only by three-dimensional measurement [14]. This approach significantly accelerates computational speed and has been widely adopted. In addition to the geometric optics model,

* Corresponding authors.
E-mail addresses: njustgel@njust.edu.cn (E. Guo), eohj@njust.edu.cn (J. Han).

https://doi.org/10.1016/j.optlaseng.2025.109100
Received 22 March 2025; Received in revised form 7 May 2025; Accepted 19 May 2025

researchers have attempted to describe the detection process of NLOS imaging at the physical level, proposing f-k boundary migration methods and virtual wave methods [15,16]. These methods can accurately model the NLOS imaging process, contributing to high-resolution imaging of complex targets.

The capability for high-resolution and fast imaging is important for the practical application of NLOS imaging. For instance, in the field of autonomous driving, the ability to observe complex scenes is critical. Considering the motion of the object and the permissible detection time, the rapid detection of target structures also holds considerable research value. However, to achieve high-resolution reconstruction results, the aforementioned methods all require dense scanning on the relay wall, resulting in a long data acquisition time that significantly limits their practical applications [14,15,19,23]. To realize fast imaging in NLOS scenarios, many methods have been proposed, including reducing the number of scanning points [24–30,23], decreasing the acquisition time per detection point [18], using single-photon avalanche diode (SPAD) array detectors combined with some modulation methods [31,32], or directly based on SPAD array detectors for scan-free imaging [33,34]. Nevertheless, a significant reduction in the number of scanning points or in the acquisition time per detection point can adversely affect image quality. Moreover, using deep learning methods to improve imaging performance can also face issues such as limited generalization capabilities of the network. The SPAD array detectors have the advantage of capturing light simultaneously from multiple pixels, the methods based on SPAD array detectors demonstrate significant advantages in detection speed. By utilizing custom-designed detector arrays in conjunction with laser scanning, current technology can achieve up to 5 frames per second (fps) [32]. If employing commercial SPAD array detector with 32×32 pixels, it is possible to achieve scan-free NLOS imaging, with the fastest acquisition speed reaching 151 fps [33,34].

Despite recent breakthroughs, achieving high-resolution real-time or near-real-time NLOS imaging remains challenging. Using array detectors instead of laser scanning offers significant advantages in terms of acquisition speed, but it also introduces some issues: crosstalk exists between pixels when using array detectors for data acquisition, resulting in a lower signal-to-noise ratio (SNR) in the collected data [33]. Current array detectors are limited in number, making dense sampling difficult, which may impose certain limitations on imaging resolution [34,14]. Furthermore, the fundamental resolution of the transient NLOS imaging is determined by the total temporal jitter of the experimental setup, which limits the spatial resolution to the centimeter scale [35,14]. In scan-free scenarios, besides the pulse width of the laser and the temporal jitter of the array detector, the influence of the field of view (FoV) of a single detection point on the temporal jitter should also be considered. In this case, the temporal jitter of the system increases, which in turn decreases the resolution of the imaging [36,6,37].

To balance imaging resolution and detection speed, this paper proposes a spatial-correlation-based scan-free NLOS imaging method called SCBSF-NLOS, which achieves high-fidelity and high-resolution reconstruction of hidden scenes while maintaining high acquisition speed. Scan-free configurations enable rapid data acquisition. Based on this, we propose a resampling method to obtain higher spatial resolution data. Considering the influence of the detection FoV on the temporal and spatial broadening of signals, the modeling for scan-free scenarios is perfected to overcome some resolution limitations. The fast acquisition speed makes the method suitable for dynamic scenes, enabling rapid imaging of the object when combined with the fast reconstruction algorithm. To better extract object information, we perform filtering in the frequency domain to remove some of the noise in the reconstruction results. Furthermore, our method can achieve high-fidelity reconstruction of target structures using an array detector with 16×16 pixels, further reducing the manufacturing cost and processing requirements of the detector.

2. Method

2.1. The forward evolution model in non-confocal scan-free scenarios

The NLOS imaging model and SCBSF-NLOS method proposed in this paper are based on the non-confocal scan-free system shown in Fig. 1(a). The following assumptions are made: there are no occlusions within the hidden scene, inter-reflections between hidden objects are not considered, and light scatters isotropically.

Let $r_1 \in \Omega_{wall} = \{(x_1, y_1, z_1) \in \mathbb{R} \times \mathbb{R} \times \mathbb{R} | z_1 = z_{wall}\}$ denote the position of the illumination point on the relay wall, and $r_2 \in \Omega_{wall} = \{(x_2, y_2, z_2) \in \mathbb{R} \times \mathbb{R} \times \mathbb{R} | z_2 = z_{wall}\}$ represents the position of the detection point corresponding to a detector pixel on the relay wall, where (x, y, z) denotes the three-dimensional space. For simplicity, assume that the relay wall is a plane at $z = z_{wall}$. The illumination point on the relay wall is fixed, and each detector pixel corresponds to a different detection point on the relay wall. For the detection point r_2, the transmission model of light from the illumination point r_1 to the hidden object and then returning to the detection point r_2 on the relay wall can be expressed as:

$$I(t, r_1, r_2) = \int_{\psi} f(s, r_1) f(s, r_2) \delta(ct - ||s - r_1|| - ||s - r_2||) ds, \tag{1}$$

where function f describes the light throughput from a point on the relay wall to a point on the hidden object, and it encompasses the bidirectional scattering distribution function, albedo, visibility, and inverse-square falloff factors [38,4]. The function δ is related to distance and propagation time, and integration is performed over time t and the hidden volume $s \in \psi = \{(x, y, z) \in \mathbb{R} \times \mathbb{R} \times \mathbb{R} | z \geqslant z_{wall}\}$.

Modeling non-confocal scenes directly is relatively complex and computationally expensive. To simplify the computational steps, we refer to the dip moveout correction [39] used in seismic imaging and propose the non-confocal transformation (NCT) correction method [34], which allows for tilted normal of the objects relative to the relay wall. By incorporating prior knowledge of the positions of the laser point and detection points, the data detected by SPAD is corrected to confocal scene data. Under the transformed confocal scenario, Equation (1) can be expressed as:

$$I'(t', r', r') = \int_{\psi} f(s, r')^2 \delta(ct' - 2||s - r'||) ds, \tag{2}$$

where $r' \in \Omega_{wall} = \{(x', y', z') \in \mathbb{R} \times \mathbb{R} \times \mathbb{R} | z' = z_{wall}\}$ is the corrected confocal point.

As shown in Fig. 1(a), in the scan-free system configuration, to ensure the detection area on the relay wall, it is necessary to use a lens to focus the detection surface of the array detector onto the relay wall, which also expands the detection FoV corresponding to a single pixel of the detector. As shown in Fig. 1, in the scan-free system, the laser spot and the detection FoV of a single pixel on the relay wall cannot be simply regarded as a point, which will affect the spatiotemporal information detected by the detector, leading to certain blurring in the object reconstruction results [6,37].

Firstly, the spatial broadening is considered. The spatial distribution of the laser spot can be represented by a two-dimensional Gaussian distribution. Assuming that the standard deviations of the two-dimensional Gaussian function are σ_x and σ_y respectively, and the central intensity is a constant P, then the light intensity at a point $r'_c = (x'_c, y'_c, z'_c = z_{wall})$ within the detection FoV can be expressed as:

$$P_c = P \underbrace{exp(-\frac{(x'_c - x')^2}{2\sigma_x^2} - \frac{(y'_c - y')^2}{2\sigma_y^2})}_{\phi_{xy}}. \tag{3}$$

The total signal I'_{space} can be expressed as the superposition of signals at each point in the detection FoV:

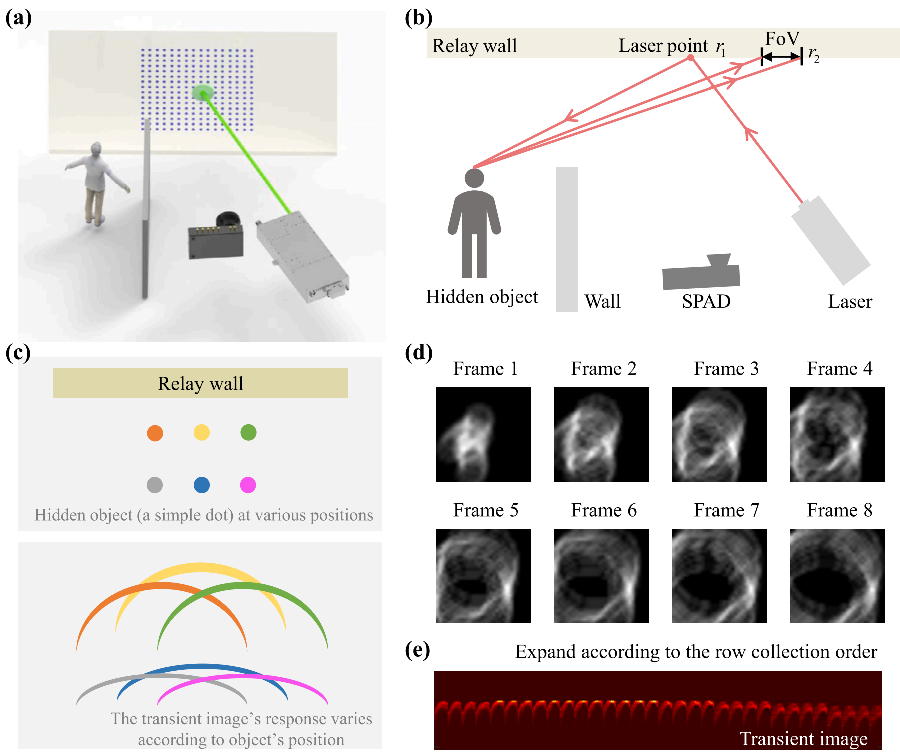

Fig. 1. Non-confocal scan-free imaging system model. (a) The optical setup of the NLOS imaging system. (b) Schematic diagram of the experiment to explain the forward evolution model. (c) A simple example illustrates that when the object is a simple dot at various positions, the transient image's response varies according to its position. (d) The two-dimensional transient images under different time bins. (e) The expanding of the collected three-dimensional transient image according to the position of the detection regions.

$$I'_{space} = P \iint [I'(x',y',z') \times \phi_{xy}]dx'_c dy'_c, \tag{4}$$

In order to facilitate the subsequent calculation, the constant P can be ignored, and I'_{space} can be written as the convolution of $I'(x',y',z')$ and ϕ_{xy}.

Subsequently, the temporal broadening is considered. The laser spot size, the detection FoV, the pulse width of the laser, and the time resolution of the detector, etc., can lead to uncertainty between the actual generation time of the signal and the ideal response time. This overall temporal broadening is denoted as σ_t, which can be determined by the half-width at half-maximum of the first echo [14,6,36]. The signal I'_{time} can be expressed as the convolution of $I'(x',y',z')$ and ϕ_t along time-axis, where $\phi_t = exp(-\frac{(t')^2}{2\sigma_t^2})$.

Considering the temporal and spatial broadening, the complete transmission model of light can be expressed as:

$$\tau' = \phi * I', \tag{5}$$

where ϕ is a shift-invariant three-dimensional blur kernel, $\phi = \phi_{xy} \cdot \phi_t$, and $*$ denotes convolution. I' represents the free-space light transmission model without considering signal broadening, which can be expressed using models from methods such as LCT or FBP. For example, when using the LCT model, $R_t\{I'\} = h * R_z\{\rho\}$. Where h is a shift-invariant three-dimensional convolution kernel, ρ represents the albedo of the hidden object, the transform R_z nonuniformly resamples and attenuates the elements of volume ρ along the z axis, and the transform R_t nonuniformly resamples and attenuates I' along the time axis [14].

In practical applications, it is necessary to establish a discrete imaging model. For a detection point of the array detector on the relay wall (i.e., $n_x = 1$ and $n_y = 1$), the detector can receive signals from the object region Ω_{xy}, $\boldsymbol{\tau}' \in \mathbb{R}_+^{n_x n_y n_t}$ and $\boldsymbol{I}' \in \mathbb{R}_+^{n_x n_y n_t}$ can be expressed as:

$$(\boldsymbol{\tau}')_j = \iint_{\Omega_{xy}} \int_{t_{j-1}}^{t_j} \tau'(x',y',t')dt'dx'dy', \tag{6}$$

$$(\boldsymbol{I}')_j = \iint_{\Omega_{xy}} \int_{t_{j-1}}^{t_j} I'(x',y',t')dt'dx'dy', \tag{7}$$

where $1 \le j \le n_t$, $\boldsymbol{\tau}'$ and $\boldsymbol{I}'$ are in vector form. Here, the transient image is defined over the time value range $[a,b] \subset (0,\infty)$, which is uniformly discretized into n_t equal spaces.

From the LCT model, the discrete free-space propagation operator can be expressed as $\boldsymbol{I}' = \boldsymbol{R}_t^{-1}\boldsymbol{H}\boldsymbol{R}_z\boldsymbol{\rho} = \boldsymbol{A}\boldsymbol{\rho}$, where matrix $\boldsymbol{H}$ is the shift-invariant three-dimensional convolution operation, $\boldsymbol{\rho} \in \mathbb{R}_+^{n_x n_y n_z}$ represents the vectorized volume of the albedo of the hidden object, and $\boldsymbol{A} = \boldsymbol{R}_t^{-1}\boldsymbol{H}\boldsymbol{R}_z$ is the light transport matrix [14]. The complete discrete imaging model can be expressed as:

$$\boldsymbol{\tau}' = \boldsymbol{\Phi}\boldsymbol{I}' = \boldsymbol{\Phi}\boldsymbol{A}\boldsymbol{\rho}, \tag{8}$$

where the matrix $\boldsymbol{\Phi} \in \mathbb{R}_+^{n_x n_y n_t \times n_x n_y n_t}$ represents the shift-invariant three-dimensional convolution operation (i.e., a convolution with a discretized version of the kernel ϕ) [14]. Computational efficiency is largely achieved using the convolution theorem to compute matrix-vector multiplications with $\boldsymbol{\Phi}$ as element-wise multiplications in the Fourier domain.

We assume that the noise model associated with the discrete model in Equation (8) satisfies:

$$\tilde{\boldsymbol{\tau}}' = \boldsymbol{\Phi}\boldsymbol{A}\boldsymbol{\rho} + \boldsymbol{\eta} = \boldsymbol{\Phi}\boldsymbol{I}' + \boldsymbol{\eta}, \tag{9}$$

where $\boldsymbol{\eta}$ represents white noise. According to the Wiener deconvolution filter [40], the solution $\boldsymbol{I}'_*$ with minimum mean square error can be expressed as [4]:

$$I'_* = F^{-1}[\frac{1}{\hat{\Phi}} \cdot \frac{|\hat{\Phi}|^2}{|\hat{\Phi}|^2 + \frac{1}{\alpha}}]F\tilde{\tau}' = F^{-1}[\frac{\hat{\Phi}^*}{|\hat{\Phi}|^2 + \frac{1}{\alpha}}]F\tilde{\tau}', \tag{10}$$

where F is the discrete Fourier transform matrix, $\hat{\Phi}$ is a diagonal matrix containing the Fourier transform of the shift-invariant three-dimensional convolution kernel, $\hat{\Phi}^*$ represents the complex conjugate of $\hat{\Phi}$, and α is a parameter that varies depending on the SNR at each frequency.

Extending Equation (10) yields the closed-form solution for NLOS imaging [4]:

$$\rho_* = A^{-1}I'_* = A^{-1}F^{-1}[\frac{\hat{\Phi}^*}{|\hat{\Phi}|^2 + \frac{1}{\alpha}}]F\tilde{\tau}', \tag{11}$$

where ρ_* is the estimated volume of the albedos of the hidden object.

2.2. Resampling method

Compared to scanning-based systems, our system uses an array detector instead of the scanning process, offering advantages in acquisition speed but inevitably introducing two new issues. First, to ensure the detection area, lens is used to focus the detection surface of the array detector onto the relay wall, which also expands the FoV for each pixel point of the detector. In Section 2.1, we consider the impact of the FoV of the detection points on imaging and incorporate the temporal and spatial broadening into the modeling process, thereby mitigating its effect on imaging. In addition, in scan-free scenarios, the number of pixels in the array detector is equivalent to the number of detection points, which affects resolution. If the number of detection points is $N \times N$, the resolution of the reconstructed object scene will be $N \times N$ [27,33]. With a fixed number of detection points, a larger detection area results in greater spacing between detection points. If this spacing exceeds the theoretical resolution, the resolution will decrease.

To achieve high-resolution imaging of hidden objects, in addition to considering the influence of the detection FoV on imaging, it is also necessary to consider the influence of a limited number of detection points on imaging resolution. To address this issue, based on the spatial correlation of the information collected from adjacent detection regions, the algorithm resampling is used to achieve fine sampling. The resampling method can obtain ToF data with higher spatial resolution, which can overcome some inherent spatial resolution limitations of the scan-free imaging systems [41–43]. Then the high-resolution reconstruction results of the hidden scenes can be obtained based on reconstruction algorithms.

As shown in Fig. 1(a), after the light undergoes diffuse reflection at the relay wall and illuminates the entire hidden object scene, the SPAD array records the ToF information of photons that are diffusely reflected from the object surface to each independent detection area on the relay wall. Most transient-based NLOS imaging methods have employed the accumulated data from the photon event histogram method for reconstruction in NLOS imaging, which requires multiple repeated acquisitions [18]. If the repeated acquisition times is too low, the time response signals collected will be insufficient, making it difficult for the final histogram obtained by statistics to fully reflect the structural information and position of the hidden objects. After repeated acquisition of K times, the accumulated photon ToF data is plotted as a histogram, and the data from different detection points are aggregated to obtain a three-dimensional spatial-temporal measurement result $\hat{Y} \in \mathbb{R}^{M\times M\times T}$ with $M \times M$ pixel size and T time bins.

As shown in Fig. 1(d), by observing the two-dimensional transient images under different time bins, it can be seen that adjacent regions exhibit similar characteristics, indicating a certain degree of spatial correlation between adjacent detection regions [44,45,25]. As shown in Fig. 1(e), when the three-dimensional transient image is expanded according to the position of the detection regions, the correlation between adjacent regions becomes evident as well. Considering the spatial correlation between adjacent detection regions, neighboring pixels typically share similar time-of-flight information. By reorganizing the data and adding new virtual detection regions between the existing detection regions, data with higher spatial resolution can be obtained. The virtual detection region partial overlaps with the existing two adjacent detection regions, and the overlap ratio of different virtual regions to the existing two adjacent detection regions is different. Based on this property, this paper proposes a method called spatial-correlation-based resampling (SCBR) method. By utilizing the spatial correlation between adjacent regions and the overlapping nature of the detection regions, the ToF information of the virtual detection regions is obtained from the low-resolution ToF data collected. This enables fine acquisition and further allows for the combination of data to obtain higher spatial resolution ToF information.

Assuming that the repeated acquisition times is K, first, the spatial-temporal measurement results obtained from the M detection regions in the first row are converted into one-dimensional data $\hat{Y}_{x1}$ according to their positions. Considering the spatial correlation between adjacent detection regions, the original M detection regions are transformed into M_{ccy} virtual detection regions, with each virtual detection region having K_{ccy} repeated acquisition times and a moving step Δk (where $\Delta k = \frac{M\times K - K_{ccy}}{M_{ccy}-1}$). Then, this operation is repeated for the data from the second to the M-th rows, and the data are converted into three-dimensional data $\hat{Y}_{x,ccy} \in \mathbb{R}^{M_{ccy}\times M\times K_{ccy}}$ according to the positions and repeated acquisition times of the virtual detection points, thereby achieving the resampling of the data along the x-axis. Subsequently, the y-axis is resampled. The spatial-temporal measurement results obtained from the M detection regions in the first column are converted to one-dimensional data $\hat{Y}_{y1}$ according to their positions. Then, the same operation used for the x-axis is applied to convert the original M detection regions into M_{ccy} virtual detection regions and apply them to each column. Finally, the resulting data are converted into three-dimensional data $\hat{Y}_{ccy} \in \mathbb{R}^{M_{ccy}\times M_{ccy}\times K_{ccy}}$, and the overall resampling process of the data is completed.

The spatial resolution of the resampled data is largely determined by the moving step size Δk. The smaller the Δk, the more virtual detection regions are obtained through resampling, resulting in higher final data spatial resolution. In the proposed scan-free imaging system, the required number of sampling points is several times the number of non-zero elements of the object [46]. When the sample quantity is insufficient, increasing the number of samplings significantly improves reconstruction performance. However, when the sampling quantity is sufficient, further increments in sampling number will lead to increased data processing and reconstruction time, with only marginal improvements in reconstruction quality. Therefore, it is necessary to consider the step size setting comprehensively. Additionally, the setting of the repeated acquisition times K_{ccy} for each virtual detection area should also consider the echo intensity of the object area. If the distance between the object and the relay wall is far, the low repeated acquisition times K_{ccy} will result in insufficient accumulation of echo photons, thereby affecting the SNR and image quality of the data.

2.3. Three-dimensional reconstruction algorithm

Using the SCBR algorithm, we can obtain a three-dimensional matrix $\hat{Y}_{ccy}$ with high spatial resolution, which subsequently leads to higher resolution reconstruction results. The overall workflow of the proposed SCBSF-NLOS method is illustrated in Fig. 2. Since the time-correlated single-photon counting of different pixels of the array detector used operates independently, it is necessary to first apply a preprocessing step to synchronize the time bins of each detection region. Subsequently, the data is resampled using the SCBR method to obtain data with higher spatial resolution. Then, based on the non-confocal ToF imaging model, the NCT algorithm is used to convert non-confocal data into confocal data. Finally, leveraging the modeling with the blur kernel and the non-confocal scan-free imaging model, the Wiener deconvolution filter

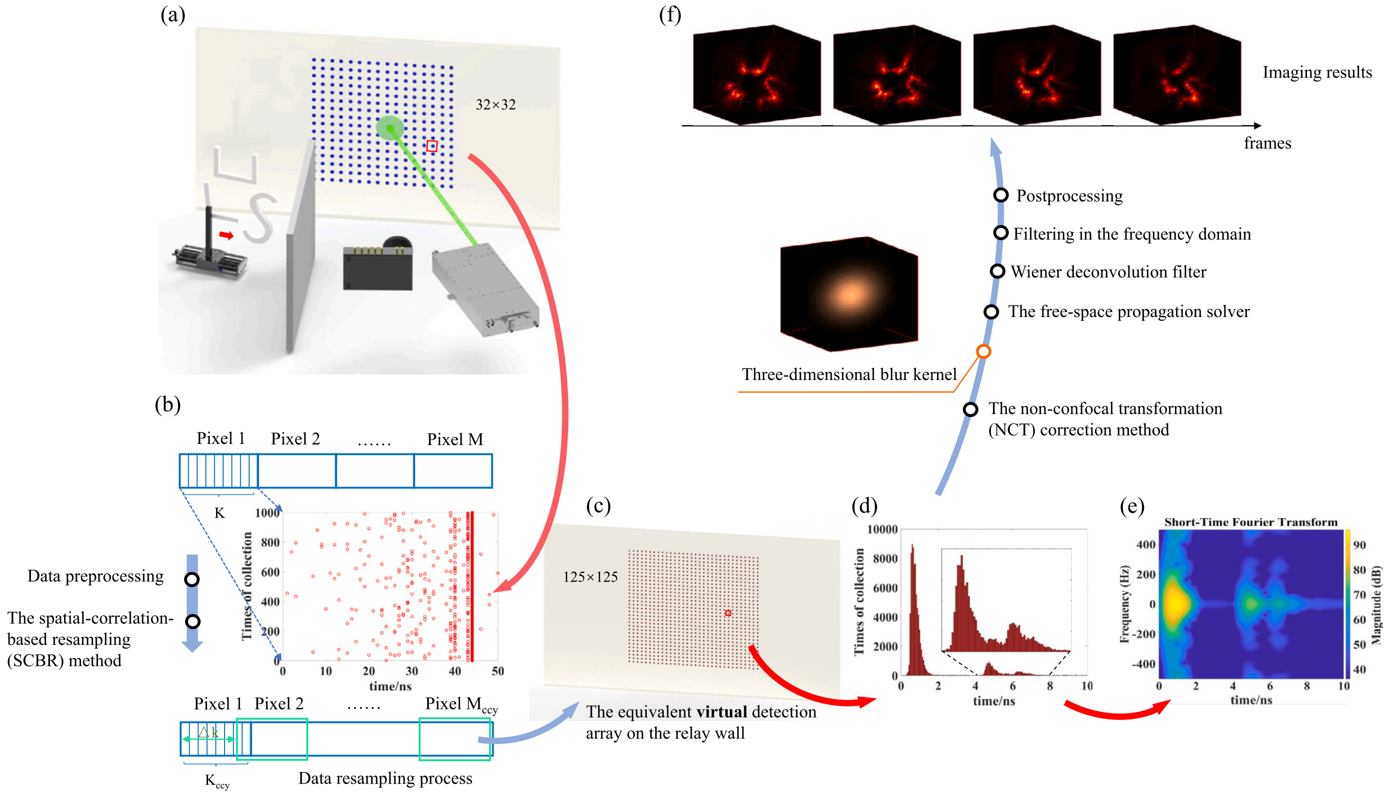

Fig. 2. The overall workflow of the SCBSF-NLOS method (a) The NLOS imaging system. (b) Data resampling process. (c) The equivalent virtual detection array on the relay wall after data resampling. (d) The histogram of the time response at one virtual detection point on the relay wall. (e) The time-frequency analysis result of the signal shown in Fig. 2(d) using short-time Fourier transform. (f) The imaging results of the dynamic scene shown in Fig. 2(a).

and the free-space propagation solver based on LCT are utilized for object reconstruction. Considering pixel crosstalk and noise interference, short-time Fourier transform is employed for time-frequency analysis. The first and secondary echo signal information is relatively rapid, and the main components of its Fourier spectrum are concentrated in the high-frequency region. The noise distribution is relatively uniform, and its main spectral components are concentrated in the low-frequency region. We perform filtering in the frequency domain to remove some of the low-frequency noise, thereby facilitating a better extraction of the object information. Then, we perform postprocessing such as grayscale stretching and obtain the three-dimensional recovery results of the object.

3. Experimental results and analysis

3.1. Experimental configuration

To experimentally validate the performance of the SCBSF-NLOS method, we established a non-confocal scan-free NLOS imaging system, the experimental setup is shown in Fig. 3. The imaging system consists of a laser, an array detector, a lens, and a narrowband filter. The high-power pulsed laser (BLAZER-GR10) emits a collimated linearly polarized beam at a wavelength of 532 nm with a repetition frequency of 20 MHz, and the laser power is adjustable with a maximum of 8 W. The polarized light is incident on the relay wall, and after one scattering, it illuminates the hidden scene. Subsequently, the hidden object in the scene scatters the light back to the relay wall. The standard transistor-transistor logic signal from the laser output can serve as the trigger signal for the array detector (Photon Force PF32-USBC-MLA-500k). The array detector focuses on the relay wall with a 6 mm lens (CHIOPT-FA0615A) or a zoom lens ranging from 1.8 mm to 3.6 mm (Edmund #55-254). The FoV is 60 cm×60 cm or 120 cm×120 cm, respectively, enabling the collection of ToF data containing object information. A narrowband filter (Thorlabs FLH532-4) is placed in front of the lens to remove most of the ambient light. The time-correlated single-photon counting of different pixels in the array detector is operated independently. The micro-lens array is added inside the detector to improve the effective detection area of pixels, thereby improving the acquisition efficiency. The system is positioned 2.1 m away from the relay wall, with the object scene hidden from the direct line of sight, and the actual power used by the laser is 1 W.

3.2. Verification experiment of the SCBSF-NLOS method

The non-confocal scan-free NLOS imaging system established in the paper utilizes a SPAD array to collect data, offering significant advantages in data acquisition speed. However, such system configuration is subject to issues like pixel crosstalk, limited detection array and considerable temporal jitter, which increase the difficulty of imaging and impose certain limitations on imaging quality and resolution. The aforementioned issues are critical factors affecting the resolution of scan-free NLOS imaging scenarios, and we propose the SCBSF-NLOS method for these three problems. To verify the imaging performance and advantages of the SCBSF-NLOS method, we perform experimental demonstrations involving multiple scenarios based on the established non-confocal scan-free NLOS imaging system.

As shown in Fig. 4, to verify the imaging capability of the proposed method in a scan-free non-confocal scenario, we compared the reconstruction results of our method with those of the filter back-projection (FBP) method [47], the array-detector-based scan-free boundary migration (SCBM) method [34], and the LCT method [14]. The hidden objects include a single character target “T”, dual-target, and a mannequin target. The detection area of the relay wall is 60 cm×60 cm, the data is collected with a spatial resolution of 32×32 and a temporal resolution of 1024, where each temporal bin spans 55 ps. As shown in the second to fourth columns of Fig. 4, we present the three-dimensional

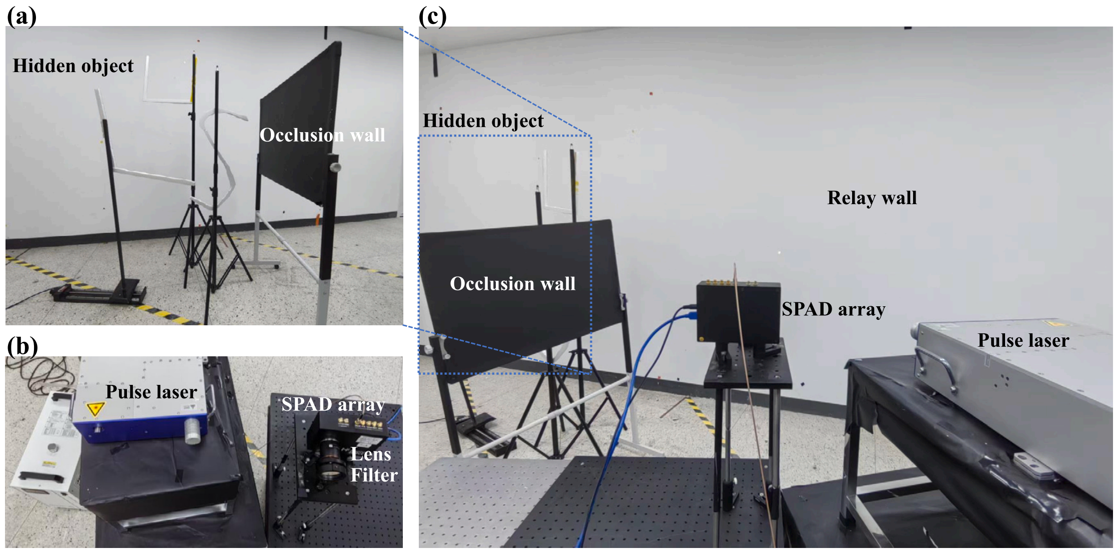

Fig. 3. Experimental setup of the non-confocal scan-free NLOS imaging system. (a) Hidden object scene. (b) Hardware configuration of the non-confocal imaging system. (c) The overall layout of the system.

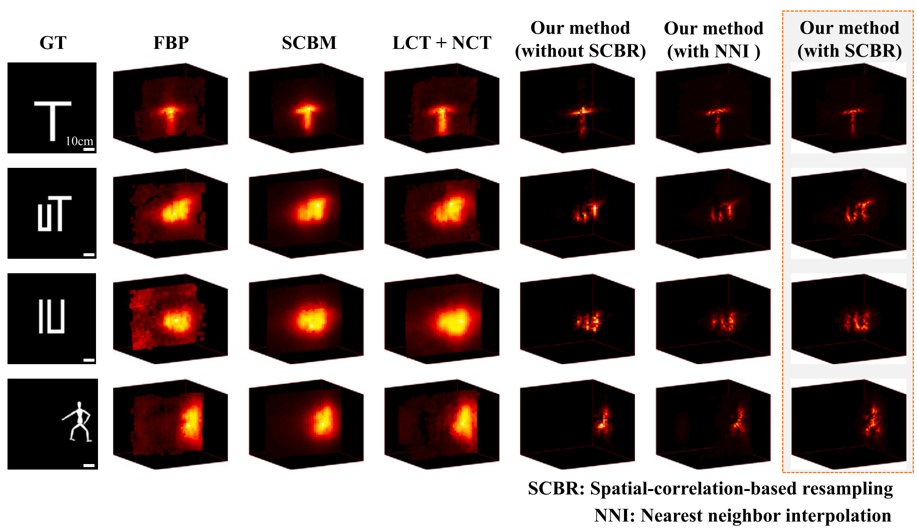

Fig. 4. Comparison of imaging effects of different methods.

reconstruction results for the FBP method, the SCBM method, and the LCT method, respectively. Since the test scenario is a non-confocal scenario, while the LCT method is suitable for confocal scenarios [14], it is necessary to first convert the non-confocal data to confocal data using the NCT method [34] before applying the LCT algorithm. By modeling the forward evolution in the scan-free scenario and considering factors such as the detection FoV that lead to temporal and spatial broadening, we propose the SCBSF-NLOS method for hidden object imaging. As shown in the fifth and seventh columns of Fig. 4, to verify the effectiveness of the resampling method SCBR, we provide comparison results with and without the resampling step. Comparing the reconstruction results of these two columns reveals that the resampling step enhances the detail imaging capability and resolution, yielding more significant improvements for complex object imaging. Additionally, we compare the super-resolution capabilities of the SCBR method and the nearest neighbor interpolation (NNI) method [27,24]. As illustrated in the last two columns of Fig. 4, it is evident that the SCBR method exhibits stronger capability in restoring details.

By comparing the reconstruction results of different methods in Fig. 4, it can be observed that the FBP method and the LCT method exhibit significant noise in their reconstruction results, which are blurry with a certain degree of structural information loss and distortion. The reconstruction performance under scan-free scenarios is thus limited. The SCBM method demonstrates good noise resistance and performs well in recovering simple hidden scenes. However, the FBP, LCT, and SCBM methods all struggle to achieve high-quality reconstruction of compact single objects or closely spaced dual-target. In comparison, our method can recover the clear structure of hidden objects and reconstruct the object with high fidelity.

In scanning-based NLOS system configuration, an increase in the scanning range of the relay wall does not induce a change in the temporal resolution of the system. The imaging resolution is related to the total scanning area on the relay wall. With the object position unchanged, the increase of the scanning area will lead to an improvement in theoretical spatial resolution [14,15]. However, for the scan-free system used in this paper, a large detection area is required to capture complete information about the hidden scene. Therefore, a lens is added in front of array detectors to magnify and focus the detection FoV onto the relay wall, the detection area on the relay wall is determined by the lens's focal length and the distance between the array detector and the re-

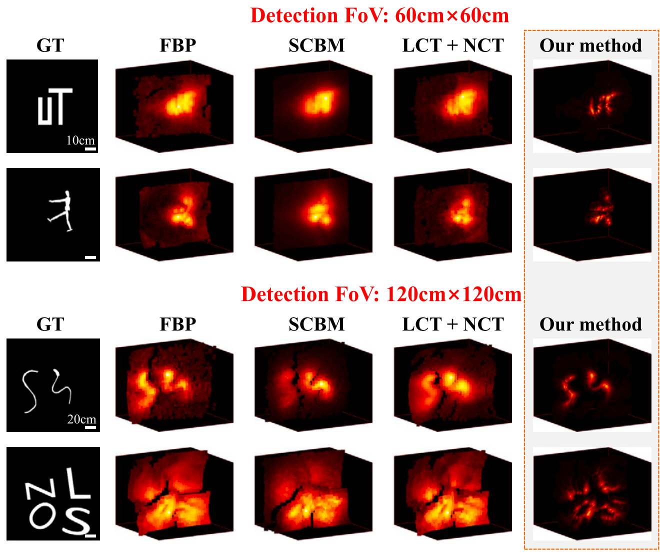

Fig. 5. Comparison of imaging effects of different methods under two different FoVs.

lay wall. However, the use of lens also expands the FoV of each pixel point on the detector, thereby impacting the spatiotemporal information detected by the system and increasing the system's temporal jitter. Therefore, for scan-free NLOS systems, a larger detection FoV does not necessarily equate to higher image quality, the detailed resolution analysis is provided in Section 3.3. The NLOS imaging forward evolution model proposed in this paper considers the impact of the FoV of the detection points on imaging and incorporates the temporal and spatial broadening into the modeling process, which is applicable to scan-free NLOS systems with varying detection FoV.

To verify the imaging and resolution capabilities of our method under different detection FoV, we tested the imaging performance and resolution at a 120 cm×120 cm FoV in addition to the 60 cm×60 cm FoV. Fig. 5 illustrates the imaging performance of different methods under these two FoVs. An increase in the detection FoV leads to an increase in the system's temporal resolution, with the total temporal jitter being 220 ps and 385 ps respectively for the two scenarios, which interferes with the imaging process. It can be observed that under both detection FoVs, the reconstruction results of the FBP, LCT, and SCBM methods exhibit significant blurring, making it difficult to recover the fine structures of the objects. If the objects are close to each other, they cannot be accurately distinguished. The method proposed in this paper effectively mitigates the impact of temporal jitter on imaging by incorporating the blur kernel derived from the modeled temporal and spatial broadening into the algorithm's convolution process. As shown in the last column of Fig. 5, our method can restore the fine features of hidden objects, enabling accurate identification of hidden scenes, and exhibits strong object reconstruction capabilities under both detection FoVs.

To more intuitively verify the imaging resolution capability of our method, we demonstrate lateral resolution tests under different detection FoVs, the results are shown in Fig. 6. From the first column to the eighth column in Fig. 6, the axial positions of the two resolution boards are kept consistent, while the lateral spacing between the two boards is reduced from 8 cm to 1 cm. When the FoV is 60 cm×60 cm and 120 cm×120 cm, the object distance from the relay wall is 40 cm and 50 cm, respectively. Considering the system temporal jitter of 220 ps and 385 ps for the two scenarios, the theoretical system resolutions are respectively calculated to be 5.5 cm and 7.52 cm, and the sampling intervals are 1.875 cm and 3.75 cm, both smaller than the theoretical system resolution. To facilitate accurate observation of the lateral reconstruction results of the object, we provide the front views of the reconstruction results for the SCBM method, the LCT method and our method instead of the three-dimensional image. From the reconstruction results, it can be seen that SCBM method and LCT method can basically achieve the theoretical system resolution. In comparison, our method incorporates temporal and spatial broadening into the overall modeling and uses a resampling algorithm to reduce the sampling interval, thereby improving the system's imaging resolution. Moreover, since our method does not require iterative optimization, it can achieve rapid high-resolution imaging of the object.

One significant advantage of the scan-free configuration is the ability to rapidly acquire object information, which offers application benefits in both dynamic scenarios and autonomous driving fields. We test the detection time required to reconstruct a relatively complex scene and the subsequent reconstruction time under two different detection FoV, and the results are presented in Fig. 7. It can be observed that the reconstruction results using the LCT method tend to be somewhat blurry, and it is difficult to accurately reconstruct complex scenes with short detection time. Our method successfully reconstructed the scene with an acquisition time of 0.0036 s, and the acquisition speed reaches 277 fps. If the acquisition time exceeds 0.0066 s, the structure of the object can be more accurately reconstructed.

Furthermore, we present a practical scenario where the detection FoV is 120 cm×120 cm. The acquisition times per frame of data are 0.0112 s and 0.1023 s respectively. The hidden scene contains three-character targets: "U" and "S" are stationary, while "L" is fixed on a displacement stage for directional movement. We collect four states in the movement process, and the reconstruction results of the hidden scenes are shown in Fig. 8. Our custom software is responsible for reading data from the hardware, processing and resampling the data, performing image reconstruction, and displaying the reconstructed images on the screen. The software runs on the MATLAB platform and operates with three parallel threads for computation. The majority of the data processing and resampling process utilize matrix calculations, with some processes incorporating GPU acceleration. By cyclically collecting and reconstructing data 100 times using different methods, we obtain the average time for each method, as indicated in the penultimate row of Fig. 8. Using the LCT algorithm for reconstruction results in relatively blurry images with significant noise. We integrate the LCT algorithm into our custom software and utilize multi-threading to accelerate the computation process. When the repetition time of each frame's data is 1000, the total time for collecting and reconstructing 100 frames is 5.07 s, averaging 0.0507 s per frame, which enables real-time imaging. Our method can better restore the structure of hidden objects, but it also leads to varying degrees of reduction in the imaging speed. Without the resampling step, when the repetition time of each frame is 1000, the total time for collecting and reconstructing 100 frames is 5.68 s, with an average of 0.0568 s per frame, achieving an imaging speed of 17 fps, which enables real-time imaging, albeit with some loss of object structural details. When the repetition time of each frame is 10000, the total time for 100 frames is 27.20 s, with an average of 0.2720 s per frame, allowing for high-fidelity imaging of the object. If the resampling step is employed, the detail information of the object can be further enhanced, but this will also increase the overall reconstruction time. For example, if the spatial resolution of the data is increased to 63×63, and the repetition time of each frame is 1000, the total reconstruction time for 100 frames of data is 19.80 s, with an average of 0.1980 s per frame, achieving an imaging rate of 5 fps, which can essentially achieve real-time imaging. In practical applications, one can choose whether to use the resampling step based on the complexity of the object scene and time constraints. Generally, selecting repeat collection 1000 time and increasing the spatial resolution to 63×63 can restore the basic structural information of the object while maintaining real-time imaging.

Our method also reduces the requirement for the number of detector pixels. As shown in Fig. 9, by maintaining a constant FoV area on the relay wall and performing spatial down-sampling on the acquired data, detection pixels are selected at equal intervals in both the horizontal and vertical directions on the detector to obtain data with a spatial res-

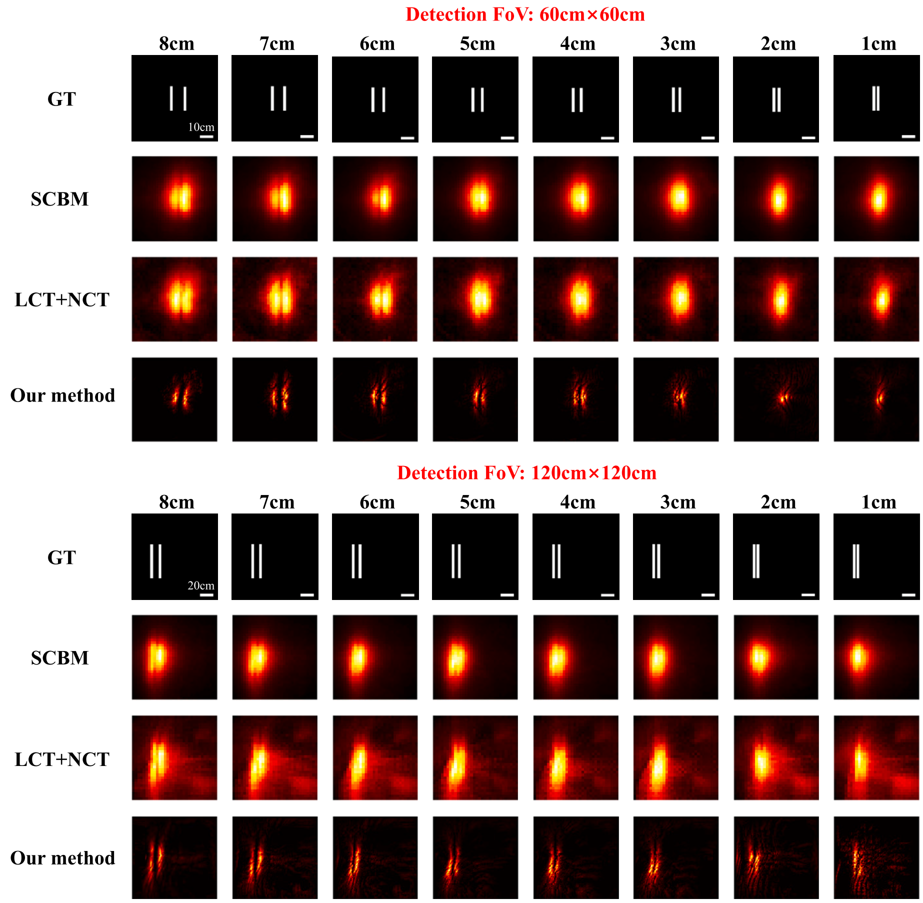

Fig. 6. Lateral resolution tests under different detection FoVs.

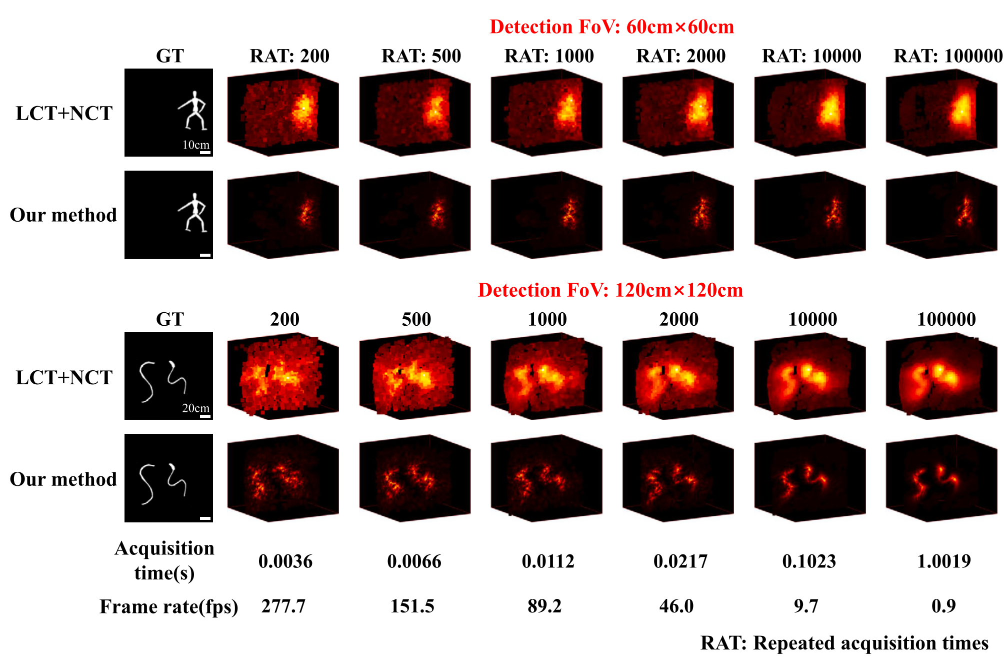

Fig. 7. The influence of acquisition time on imaging. The number at the top of the reconstruction results is the repetition time during the acquisition.

olution of 16×16. Different reconstruction algorithms are then applied for the recovery of hidden scenes, with the results displayed in Fig. 9. It can be observed that FBP, SCBM, and LCT struggle to recover structural details of the object and can only perform basic imaging on simple structures. After using the resampling step to increase the spatial resolution of the data to 121×121, our method can accurately recover the structural details of the object with different complexity. Consequently, our method is applicable to detectors with a pixel array of 16×16, further reducing the manufacturing cost and process requirements for detectors. We also compared the super-resolution capabilities of the SCBR method

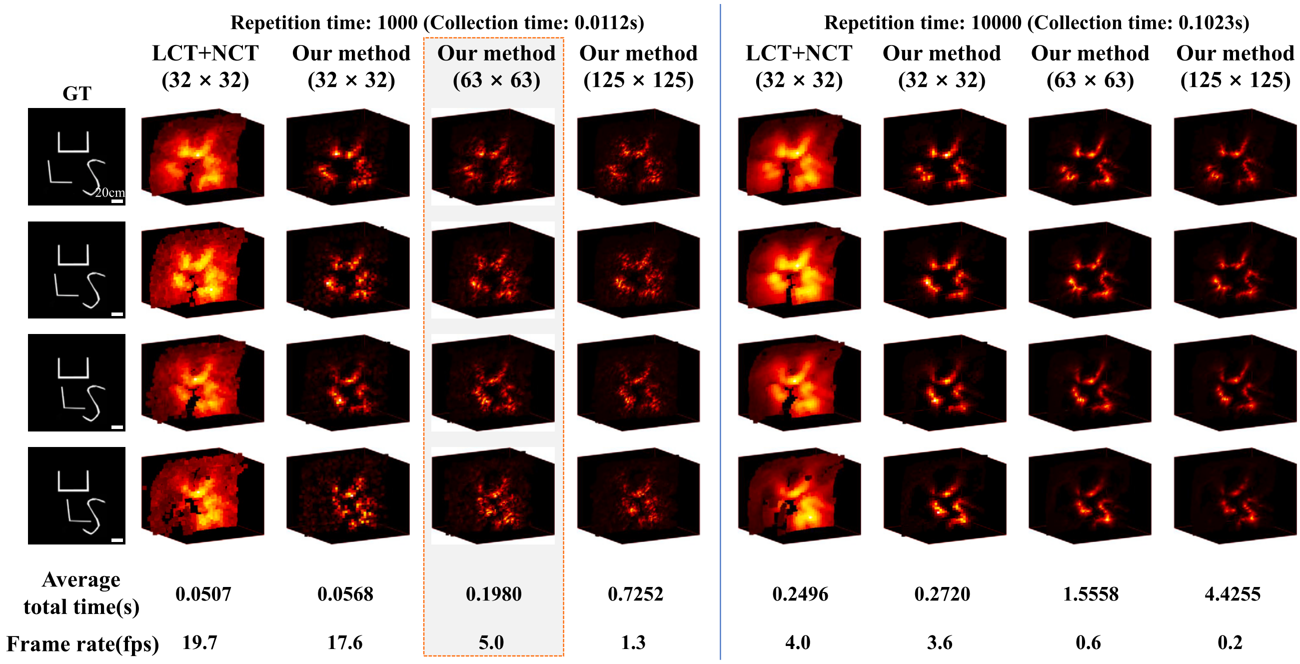

Fig. 8. Comparison of imaging speed of different methods.

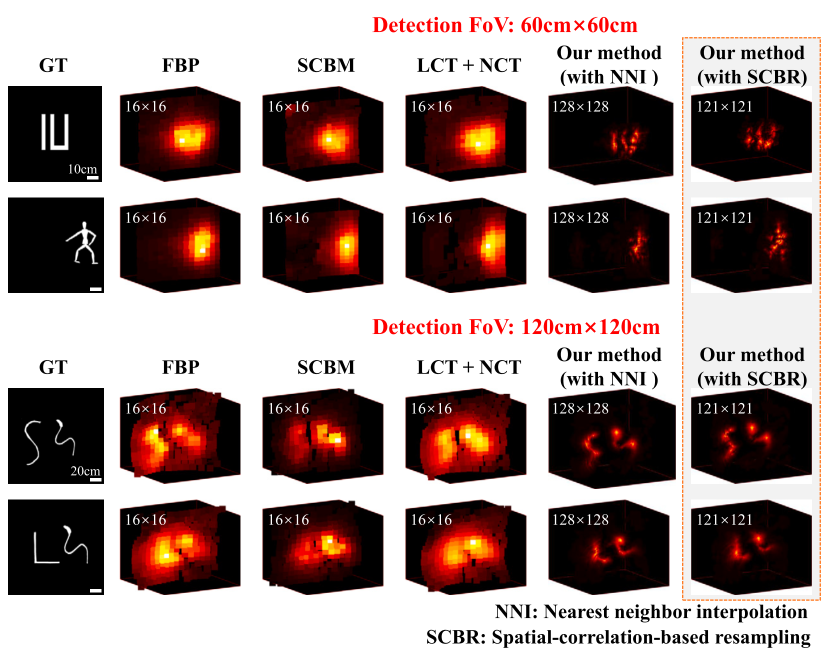

Fig. 9. Imaging based on data with spatial resolution of 16×16.

and the NNI method, as shown in the last two columns of Fig. 9, revealing the advantage of the SCBR method in detail recovery.

3.3. *The imaging resolution analysis of the scan-free NLOS system*

In practical applications of NLOS imaging, if it is desired to resolve two points in the object scene spatially, it is first necessary that their indirect signals be temporally resolvable [14]. This means that the difference in arrival times of the two time-resolved signals Δt must be greater than the full width at half maximum of the system's overall temporal jitter γ:

$$\Delta t \geq \gamma. \tag{12}$$

Where

$$\gamma = 2\sqrt{2\ln 2}\sigma_t, \tag{13}$$

σ_t is the standard deviation of the overall temporal jitter of the system. Therefore, the minimum axial distance Δz along the z-axis needs to satisfy:

$$\Delta z \geq \frac{c \cdot \Delta t}{2} \geq c \cdot \sqrt{2\ln 2}\sigma_t. \tag{14}$$

If the lateral resolution Δx is much less than the overall detection area $2w \times 2w$ on the relay wall, then:

$$\frac{c \cdot \Delta t}{2} \approx \Delta x \cos(\theta) \approx \Delta x \cos(\tan^{-1}(\frac{z}{w})) = \frac{\Delta x \cdot w}{\sqrt{w^2 + z^2}}. \tag{15}$$

The range of Δx can be determined by referring to Equation (12):

$$\Delta x \geq \frac{c \cdot \sqrt{w^2 + z^2}}{w} \cdot \sqrt{2 \ln 2}\sigma_t. \tag{16}$$

Therefore, in a scan-free NLOS imaging system, the theoretical spatial resolution of the system is influenced by the system's temporal jitter, the overall detection area of $2w \times 2w$, and the distance z between the hidden object and the relay wall. The smaller the system's time jitter and the closer the object is to the relay wall, the smaller the value of Δx.

However, in the scan-free system configuration, the spatial resolution of the imaging is not completely positively correlated with the detection area. In the case that the position of the system and the relay wall remains unchanged, to increase the detection FoV on the relay wall, it is necessary to replace the lens with a smaller focal length, which will also expand the FoV of individual pixels. In practical scenarios, the FoV range of the detection points can affect the spatiotemporal information captured by the detector. An increased FoV will also lead to an increase in system time jitter, resulting in some blurring in the object reconstruction results [6].

Additionally, during actual data collection, the number of samples will affect the lateral resolution. For NLOS imaging based on an array detector, if the detector has a pixel count of N×N, then the spatial resolution of the reconstructed object scene will also be N×N [27,33,34]. To achieve theoretical resolution in practical reconstruction and avoid aliasing, the spacing between detection positions on the wall should be less than Δx [15]. In scan-free NLOS imaging systems, the pixel count of the array detector determines the number of detection points. With a fixed number of detection points, a larger detection area results in greater spacing between them. If the detection spacing exceeds the theoretical resolution, the actual resolution will decrease.

4. Discussion

According to the theoretical analysis and experimental demonstration, several discussions are clarified as follows:

(i) To achieve rapid NLOS imaging, this paper employs a scan-free configuration to achieve data acquisition. However, such a system configuration is subject to limitations including a limited detection array, significant temporal jitter, and pixel crosstalk, which impose certain constraints on image quality and resolution. This paper proposes the data resampling method SCBR, which leverages the spatial correlation of information in adjacent detection regions to overcome device limitations and obtain high-resolution data. Considering the impact of signal temporal and spatial broadening, by incorporating the blur kernel derived from the modeled temporal and spatial broadening into the algorithm's convolution process, the effect of temporal jitter on imaging can be effectively mitigated, thereby restoring the fine features of hidden objects. Considering pixel crosstalk and noise interference, frequency-domain filtering based on time-frequency analysis can be used to remove some low-frequency noise, thus better extracting object information.

(ii) We develop a non-confocal scan-free imaging system to validate the effectiveness of the proposed method. The experimental results demonstrate that our method can achieve the reconstruction of hidden scenes with a detection time of only 0.0036 s. Compared to the SCBM method, our approach represents a breakthrough in both probing time and scene complexity. The background stability afforded by rapid acquisition enables our method to be suitable for dynamic scenes, allowing for high-resolution NLOS imaging of dynamic NLOS scenarios, with an imaging speed of 5 fps.

(iii) For scan-free NLOS systems, a larger detection field of view does not necessarily equate to higher imaging quality. An increased detection FoV not only enlarges the sampled area but also expands the FoV for each pixel on the detector, thereby affecting the temporal and spatial information detected. The NLOS imaging forward evolution model proposed in this paper considers the impact of the FoV of the detection points on imaging and incorporates the temporal and spatial broadening into the modeling process, which is applicable to scan-free NLOS systems with varying detection FoV. Additionally, the resampling step enhances the spatial resolution of the data, allowing the proposed method to be applicable to detectors with a pixel array of 16×16, further reducing the manufacturing cost and process requirements for the detectors.

5. Conclusion

Real-time imaging capability has always been crucial for the practicality of NLOS imaging. This paper employs a scan-free configuration to achieve rapid data acquisition, with a maximum acquisition rate of up to 277 fps. To address issues inherent in scan-free system configurations, such as limited detection arrays, significant time jitter, and pixel crosstalk, a spatial-correlation-based scan-free NLOS imaging method called SCBSF-NLOS is proposed. This method improves the lateral resolution to 2 cm and facilitates the reconstruction of more complex dynamic scenes. Without the resampling step, the imaging speed of this method reaches 17 fps, allowing for real-time imaging of complex scenes. By incorporating the resampling step, the imaging details can be further improved, achieving high-resolution reconstructions of dynamic NLOS scenes at 5 fps, which holds significant value for various practical applications.

CRediT authorship contribution statement

Wenjun Zhang: Writing – review & editing, Writing – original draft, Software, Methodology, Investigation, Formal analysis, Data curation, Conceptualization. **Shuo Zhu:** Writing – review & editing, Supervision. **Lijia Chen:** Formal analysis, Data curation. **Lianfa Bai:** Supervision, Resources, Funding acquisition. **Edmund Y. Lam:** Writing – review & editing. **Enlai Guo:** Supervision, Resources, Project administration, Funding acquisition. **Jing Han:** Supervision, Resources, Project administration, Funding acquisition, Conceptualization.

Declaration of competing interest

The authors declare that they have no known competing financial interests or personal relationships that could have appeared to influence the work reported in this paper.

Acknowledgements

This work was supported by the National Natural Science Foundation of China (62427803, 62031018, U23A20283), Jiangsu Provincial Key Research and Development Program (BE2022391) and the Fundamental Research Funds for the Central Universities (30924010812).

Data availability

Data will be made available on request.

References

[1] Isogawa M, Yuan Y, O'Toole M, Kitani K. Optical non-line-of-sight physics-based 3d human pose estimation. In: 2020 IEEE/CVF conference on computer vision and pattern recognition (CVPR); 2020. p. 7011–20.

[2] Scheiner N, Kraus F, Wei F, Phan B, Mannan F, Appenrodt N, et al. Seeing around street corners: non-line-of-sight detection and tracking in-the-wild using Doppler radar. In: 2020 IEEE/CVF conference on computer vision and pattern recognition (CVPR); 2020. p. 2065–74.

[3] Chan S, Warburton RE, Gariepy G, Leach J, Faccio D. Non-line-of-sight tracking of people at long range. Opt Express 2017;25(9):10109–17.

[4] Lindell DB, Wetzstein G. Three-dimensional imaging through scattering media based on confocal diffuse tomography. Nat Commun 2020;11(1):4517.

[5] Chen W, Wei F, Kutulakos KN, Rusinkiewicz S, Heide F. Learned feature embeddings for non-line-of-sight imaging and recognition. ACM Trans Graph 2020;39(6):1–18.

[6] Wu C, Liu J, Huang X, Li Z-P, Yu C, Ye J-T, et al. Non-line-of-sight imaging over 1.43 km. Proc Natl Acad Sci 2021;118(10):e2024468118.

[7] Zhu S, Ge Z, Wang C, Han J, Lam EY. Efficient non-line-of-sight tracking with computational neuromorphic imaging. Opt Lett 2024;49(13):3584–7.

[8] Katz O, Heidmann P, Fink M, Gigan S. Non-invasive single-shot imaging through scattering layers and around corners via speckle correlations. Nat Photonics 2014;8(10):784–90.

[9] Metzler CA, Heide F, Rangarajan P, Balaji MM, Viswanath A, Veeraraghavan A, et al. Deep-inverse correlography: towards real-time high-resolution non-line-of-sight imaging. Optica 2020;7(1):63–71.

[10] Cao R, de Goumoens F, Blochet B, Xu J, Yang C. High-resolution non-line-of-sight imaging employing active focusing. Nat Photonics 2022;16:462–8.

[11] Lindell DB, Wetzstein G, Koltun V. Acoustic non-line-of-sight imaging. In: 2019 IEEE/CVF conference on computer vision and pattern recognition (CVPR); 2019. p. 6773–82.

[12] Maeda T, Wang Y, Raskar R, Kadambi A. Thermal non-line-of-sight imaging. In: 2019 IEEE international conference on computational photography (ICCP); 2019. p. 1–11.

[13] Velten A, Willwacher T, Gupta O, Veeraraghavan A, Bawendi MG, Raskar R. Recovering three-dimensional shape around a corner using ultrafast time-of-flight imaging. Nat Commun 2012;3(1):745.

[14] O'Toole M, Lindell DB, Wetzstein G. Confocal non-line-of-sight imaging based on the light-cone transform. Nature 2018;555(7696):338–41.

[15] Lindell DB, Wetzstein G, O'Toole M. Wave-based non-line-of-sight imaging using fast fk migration. ACM Trans Graph 2019;38(4):1–13.

[16] Liu X, Guillén I, La Manna M, Nam JH, Reza SA, Le T Huu, et al. Non-line-of-sight imaging using phasor-field virtual wave optics. Nature 2019;572(7771):620–3.

[17] Liu X, Wang J, Xiao L, Shi Z, Fu X, Qiu L. Non-line-of-sight imaging with arbitrary illumination and detection pattern. Nat Commun 2023;14(1).

[18] Li Z, Liu X, Wang J, Shi Z, Qiu L, Fu X. Fast non-line-of-sight imaging based on first photon event stamping. Opt Lett 2022;47(8):1928–31.

[19] Liu X, Bauer S, Velten A. Phasor field diffraction based reconstruction for fast non-line-of-sight imaging systems. Nat Commun 2020;11(1):1645.

[20] O'Toole M, Heide F, Xiao L, Hullin MB, Heidrich W, Kutulakos KN. Temporal frequency probing for 5d transient analysis of global light transport. ACM Trans Graph 2014;33(4):1–11.

[21] La Manna M, Kine F, Breitbach E, Jackson J, Sultan T, Velten A. Error backprojection algorithms for non-line-of-sight imaging. IEEE Trans Pattern Anal Mach Intell 2019;41(7):1615–26.

[22] Arellano V, Gutierrez D, Jarabo A. Fast back-projection for non-line of sight reconstruction. In: ACM SIGGRAPH 2017 posters; 2017. p. 1–2.

[23] Ye J, Sun Y, Li W, Zeng J-W, Hong Y, Li Z-P, et al. Real-time non-line-of-sight computational imaging using spectrum filtering and motion compensation. Nat Comput Sci 2024;4(12):920–7.

[24] Wang J, Liu X, Xiao L, Shi Z, Qiu L, Fu X. Non-line-of-sight imaging with signal superresolution network. In: 2023 IEEE/CVF conference on computer vision and pattern recognition (CVPR); 2023. p. 17420–9.

[25] Zhao Z, Zhang Q, Li X, Guo Y, Pu M, Zhang F, et al. High-resolution non-line-of-sight imaging based on liquid crystal planar optical elements. Nanophotonics 2024.

[26] Isogawa M, Chan D, Yuan Y, Kitani K, O'Toole M. Efficient non-line-of-sight imaging from transient sinograms. In: Computer vision – ECCV 2020; 2020. p. 193–208.

[27] Ye J-T, Huang X, Li Z-P, Xu F. Compressed sensing for active non-line-of-sight imaging. Opt Express 2021;29(2):1749–63.

[28] Ding R, Ye J, Gao Q, Xu F, Duan Y. Curvature regularization for non-line-of-sight imaging from under-sampled data. IEEE Trans Pattern Anal Mach Intell 2024;46(12):8474–85.

[29] Liu X, Wang J, Xiao L, Fu X, Qiu L, Shi Z. Few-shot non-line-of-sight imaging with signal-surface collaborative regularization. In: 2023 IEEE/CVF conference on computer vision and pattern recognition (CVPR); 2023. p. 13303–12.

[30] Zhu S, Sua YM, Bu T, Huang Y-P. Compressive non-line-of-sight imaging with deep learning. Phys Rev Appl 2023;19(3):034090.

[31] Yang W, Zhang C, Jiang W, Zhang Z, Sun B. None-line-of-sight imaging enhanced with spatial multiplexing. Opt Express 2022;30(4):5855–67.

[32] Nam JH, Brandt E, Bauer S, Liu X, Renna M, Tosi A, et al. Low-latency time-of-flight non-line-of-sight imaging at 5 frames per second. Nat Commun 2021;12(1):6526.

[33] Pei C, Zhang A, Deng Y, Xu F, Wu J, Li DU-L, et al. Dynamic non-line-of-sight imaging system based on the optimization of point spread functions. Opt Express 2021;29(20):32349–64.

[34] Zhang W, Guo E, Zhu S, Huang C, Chen L, Liu L, et al. Real-time scan-free non-line-of-sight imaging. APL Photon 2024;9(12):126101.

[35] Wang B, Zheng M-Y, Han J-J, Huang X, Xie X-P, Xu F, et al. Non-line-of-sight imaging with picosecond temporal resolution. Phys Rev Lett 2021;127:053602.

[36] Wang D, Hao W, Tian Y, Xu W, Tian Y, Cheng H, et al. Enhancing the spatial resolution of time-of-flight based non-line-of-sight imaging via instrument response function deconvolution. Opt Express 2024;32(7):12303–17.

[37] O'Toole M, Heide F, Lindell DB, Zang K, Diamond S, Wetzstein G. Reconstructing transient images from single-photon sensors. In: 2017 IEEE conference on computer vision and pattern recognition (CVPR); 2017. p. 2289–97.

[38] Xin S, Nousias S, Kutulakos KN, Sankaranarayanan AC, Narasimhan SG, Gkioulekas I. A theory of Fermat paths for non-line-of-sight shape reconstruction. In: 2019 IEEE/CVF conference on computer vision and pattern recognition (CVPR); 2019. p. 6793–802.

[39] Yilmaz Ö. Seismic data analysis: Processing, inversion, and interpretation of seismic data. Society of Exploration Geophysicists. 2001.

[40] Wiener N. Extrapolation, interpolation, and smoothing of stationary time series: with engineering applications. The MIT Press; 1949.

[41] Farsiu S, Robinson D, Elad M, Milanfar P. Advances and challenges in super-resolution. Int J Imaging Syst Technol 2004;14(2):47–57.

[42] Sun M jie, Edgar MP, Phillips DB, Gibson GM, Padgett MJ. Improving the signal-to-noise ratio of single-pixel imaging using digital microscanning. Opt Express 2016;24(10):10476–85.

[43] Jiang Y, Liu B, Wang R, Chen Y, Chen Z, Zhao B, et al. Enhancing angular resolution in single-photon lidar for daytime long-range 3d imaging. Opt Lasers Eng 2024;178:108178.

[44] Tachella J, Altmann Y, Ren X, McCarthy A, Buller GS, McLaughlin S, et al. Bayesian 3d reconstruction of complex scenes from single-photon lidar data. SIAM J Imaging Sci 2019;12(1):521–50.

[45] Halimi A, Tobin R, McCarthy A, Bioucas-Dias J, McLaughlin S, Buller GS. Robust restoration of sparse multidimensional single-photon lidar images. IEEE Trans Comput Imaging 2020;6:138–52.

[46] Jiang X, Raskutti G, Willett R. Minimax optimal rates for Poisson inverse problems with physical constraints. IEEE Trans Inf Theory 2015;61(8):4458–74.

[47] Laurenzis M, Velten A. Feature selection and back-projection algorithms for non-line-of-sight laser–gated viewing. J Electron Imaging 2014;23(6):063003.